In: AIAA Aviation Forum and Ascend 2025, 21-25 July 2025, Las Vegas, USA, Article number 2025-3371
DOI: 10.2514/6.2025-3371

Energy Comparison in Terminal Area for Narrow Body, SAF and LH2 Aircraft

N. Kang[1], J. Cha[2], D. Judt[3], C. Lawson[4] and M. Skote[5]
Cranfield University, Bedford, MK43 0AL, United Kingdom

D. Reid[6]
Airbus Operations Ltd, Bristol, BS34 7PA, United Kingdom

The aviation industry is transitioning towards sustainable propulsion technologies to address stringent environmental targets and rising operational demands. This study evaluates actuator energy requirements in terminal phase for three narrow-body aircraft architectures: a conventional A320-like platform, a more-electric aircraft powered by Sustainable Aviation Fuel (SAF), and a Liquid Hydrogen (LH_2) concept. Detailed actuator models for electro-mechanical and servo-hydraulic systems were developed and integrated into mission-level simulations to capture power and energy profiles across key subsystems, including high-lift devices, landing gear, spoilers, brakes, and steering. Results show that while the baseline aircraft consumes the most energy due to hydraulic inefficiencies, the SAF and LH_2 configurations demonstrate notable reductions in actuator energy demands. The findings highlight how system-level electrification and architectural innovations can enhance terminal efficiency, paving the way for greener, high-performance single-aisle aircraft.

I. Nomenclature

A	=	amplitude of oscillation
B	=	wheel footprint width
D	=	drag force
D_{LG}	=	distance from main landing gear to centreline
d_{travel}	=	travel distance
F_z	=	normal force
g	=	gravitational constant
L	=	lift force
$L_{\mathrm{wheelbase}}$	=	distance from nose landing gear to main landing gear
M	=	moment
m_{MTOW}	=	aircraft maximum take-off mass
S	=	sideload
T	=	thrust force
T_{idle}	=	idle thrust force
T_R	=	reverse thrust force
η_{NLG}	=	percent of maximum take-off weight load on main landing gear
μ	=	rolling coefficient

[1] PhD Student, Centre for Aeronautics, namuk.kang@cranfield.ac.uk
[2] Research Fellow, Centre for Aeronautics, Jihyoung.Cha@cranfield.ac.uk
[3] Senior Lecturer, Centre for Aeronautics, david.judt@cranfield.ac.uk
[4] Reader, Centre for Aeronautics, c.p.lawson@cranfield.ac.uk
[5] Professor, Centre for Aeronautics, M.Skote@cranfield.ac.uk
[6] Senior Engineer, Airbus, david.reid@airbus.com

Published by AIAA. This is the Author Accepted Manuscript issued with: Creative Commons Attribution License (CC:BY 4.0).
The final published version (version of record) is available online at DOI:10.2514/6.2025-3371. Please refer to any applicable publisher terms of use.

II. Introduction

The aviation industry is undergoing a transformative shift to address mounting environmental challenges while meeting the increasing demand for air travel [1]. The next generation of commercial aircraft platforms aims to leverage advanced technologies, such as high-voltage electrical power distribution networks, to support zero-emission propulsion systems and reduce overall energy consumption [2]. Future propulsion solutions, including SAF and LH_2, have emerged as promising pathways for achieving significant reductions in carbon emissions and improving energy efficiency. In line with the electrification trend, SAF and LH_2 aircraft adopt Electro-Mechanical Actuators (EMAs), eliminating the need for conventional centralised hydraulic power systems [3]. This study presents an estimation of energy consumption for EMAs, particularly during terminal flight phases, and provides a comparative analysis with conventional hydraulic actuators.

To ensure efficient operations in future high-density terminal areas, it is crucial to address current challenges, including energy conservation, with particular emphasis on optimising terminal area energy use [4]. Crucial aspects for terminal energy estimation include the operational dynamics of actuators governing the high-lift system, spoilers, steering, braking, and landing gear deployment. Past work [5] estimated fuel consumption during terminal phases; however, it did not extend to novel architectural systems such as those based on SAF and LH_2, which introduce fundamentally different system integration and energy management strategies. Detailed power estimation for both conventional and novel actuator systems, such as hydraulic actuator and EMAs, has been studied [6], however, with a focus on the primary flight control systems, including the elevator, rudder, and aileron. Conventional and electric subsystem actuation systems have also been analysed for control surfaces and landing gear systems across entire operational mission scenarios, providing insights into system-level design trade-offs. However, these studies generally focused on configuration and sizing considerations rather than detailed power and energy consumption estimates during specific flight phases such as taxiing or landing [7]. Notably, the integration of high-fidelity actuator modeling into mission-level simulations, as demonstrated by the study [8], underscores the importance of evaluating actuator performance under realistic, time-resolved flight scenarios. However, the scope of their analysis was limited to small all-electric aircraft, and did not address the unique system complexities or energy implications of narrow body platforms.

Such past work did not encompass the power and energy aspects of high-lift device systems and landing gear systems of single-aisle aircrafts. To address these gaps, this study focuses on the power and energy requirements of A320-like baseline, SAF and LH_2-based single-aisle aircraft platforms, specifically during terminal flight phases such as landing, taxiing, and the operation of high-lift devices. By analysing the SAF and LH_2 platforms in comparison with a baseline aircraft, key differences in energy demands are identified, driven by variations in aircraft weight, aerodynamic characteristics, and system architectures. This paper begins with a description of the three aircraft models used in the study. Following this, the methodology for actuator characteristics modelling is outlined. The paper then presents the energy requirements during terminal flight phases, based on the simulation results for each aircraft configuration.

III. Aircraft Model Description

This study investigates and compares actuator system architectures across three representative aircraft configurations. The comparative analysis focuses on energy requirements during terminal flight phases where actuator usage becomes concentrated due to frequent deployment of high-lift devices, spoilers, and landing gear. The first narrow body baseline model referred to the A320-200 WV000, representing the initial weight variant of the A320 series. It is illustrated in Figure 1 and serves as the reference for conventional aircraft employing a centralised hydraulic system. For advanced configurations, the A-23 Theseus, depicted in Figure 2, is a conceptual sustainable aviation fuel (SAF)-powered narrowbody aircraft developed by Cranfield, as part of the Clean Aviation initiative. It is representative of a more-electric aircraft (MEA) architecture, replacing traditional hydraulics with distributed EMAs for flight controls, landing gear, and high-lift systems. The FZN-1E, shown in Figure 3, part of the FlyZero programme led by the Aerospace Technology Institute (ATI) and funded by the UK Government, is a zero-carbon narrowbody concept powered by liquid hydrogen. Developed in partnership with a UK-wide industrial and academic consortium including Eaton, Cranfield University, and GKN Aerospace, the FZN-1E was created to explore the feasibility of a transonic hydrogen-fuelled aircraft for service entry by the 2030s. It features aft-mounted gas turbine engines adapted for hydrogen combustion, with cryogenic tanks housed in the rear fuselage. The FZN-1E incorporates a fully electric actuation architecture, aligned with its zero-emission objectives and tailored to support novel system integration. Table 1 summarises the principal geometric, inertial, and performance characteristics of the A320-200, A-23 Theseus, and FZN-1E aircraft models used in this study; in accordance with methods outlined in [9-10].



Fig 1. A320-like for baseline.



Fig 2. A-23 Theseus for SAF.



Fig 3. FZN-1E for LH_2.

Table 1. Aircraft characteristics of A320-200, A-23 and FZN-1E

Characteristic	A320-200		A-23 Theseus		FZN-1E	
	Imperial	Metric	Imperial	Metric	Imperial	Metric
Max gross weight	162,040 lb	73,500 kg	210,548 lb	95,500 kg	155,913 lb	70,700 kg
Roll inertia, I_{xx}	1.09×10^6 slug ft^2	1.47×10^6 kg m^2	1.98×10^6 slug ft^2	2.69×10^6 kg m^2	1.26×10^6 slug ft^2	1.71×10^6 kg m^2
Pitch inertia, I_{yy}	2.76×10^6 slug ft^2	3.75×10^6 kg m^2	5.79×10^6 slug ft^2	7.84×10^6 kg m^2	3.78×10^6 slug ft^2	5.12×10^6 kg m^2
Yaw inertia, I_{zz}	3.86×10^6 slug ft^2	5.23×10^6 kg m^2	7.57×10^6 slug ft^2	10.26×10^6 kg m^2	4.88×10^6 slug ft^2	6.61×10^6 kg m^2
Wingspan	117.45 ft	35.80 m	139.27 ft	42.45 m	128.94 ft	39.30 m
Length	123.29 ft	37.57 m	156.56 ft	47.70 m	147.01 ft	44.80 m
Height	38.61 ft	11.76 m	39.37 ft	12.00 m	33.46 ft	10.20 m
Range	2,700 nm	5,000 km	3,500 nm	6,482 km	2,400 nm	4,445 km
Service ceiling	39,000 ft	11,887 m	39,000 ft	11,887 m	35,000 ft	10,668 m
Cruise speed	Mach 0.78	833 km/h	Mach 0.78	833 km/h	Mach 0.78	833 km/h

IV. Actuator Characteristics

Understanding actuator power demand under terminal flight conditions is crucial for evaluating system-level efficiency and sizing onboard power sources for the A320-like narrow-body aircraft, SAF, and LH_2 aircraft configurations. All actuator models shown are developed based on the representative Electro-Servohydraulic Actuator (ESHA) and EMA characteristics in Figure 4. These characteristics are derived from the study [6], using datasheet parameters available in the public domain. The hydraulic actuation model primarily consists of linear hydraulic cylinders connected to control surfaces via moment arms. Each cylinder is equipped with a local servo valve that regulates hydraulic fluid flow from engine-driven main pumps. The system operates with a 3000 psi supply and a 50 psi return line. Energy losses in this architecture primarily arise from valve and cylinder leakage, as well as friction within the actuator assembly. In contrast, EMAs draw electrical power from an onboard bus and convert it into rotational mechanical energy via a brushless DC permanent magnet motor. This energy is then transmitted through a ball screw mechanism to produce linear motion. Energy losses in EMAs are mainly attributable to mechanical friction, electrical heating, and magnetic flux leakage. Detailed modelling of the actuators, including component-level characteristics and performance validation, can be found in the study [6].

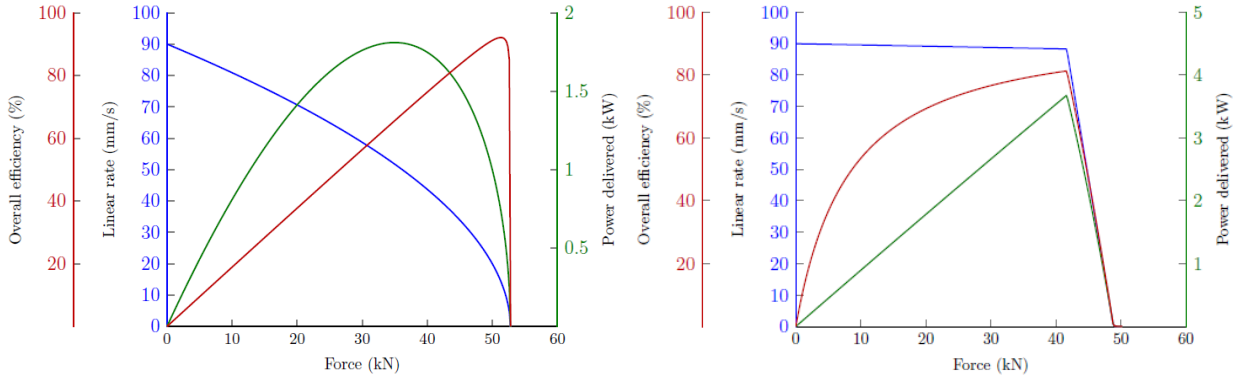


Fig 4. Load, actuator rate, efficiency, and power characteristics of ESHA (left) and EMA (right).

Figure 5 presents the overall methodology used to model actuators and ensure model fidelity across the three aircraft configurations. For the actuator modelling of high-lift devices and landing gear systems, actuator characteristics in Figure 4 underwent individual scaling adjustments to align with the actuation rate and power values at typical design load or as the maximum rate at zero load. For the hydrogen-powered FZN-1E configuration, novel systems are modelled separately. In addition to analysing actuator characteristics, this study also developed integrated models linking actuator output to control surface kinematics. As a result, investigations into linkage dynamics and gear ratio effects were conducted and are subsequently presented. Building on this, actuator models for the high-lift and landing gear systems were developed and validated against technical specifications and published academic references. All models were incorporated into a modified simulation framework, Aircraft-Level Dynamic Integrated Thermal Simulation (ALDITS), to estimate energy consumption across terminal mission segments for all three aircraft configurations.

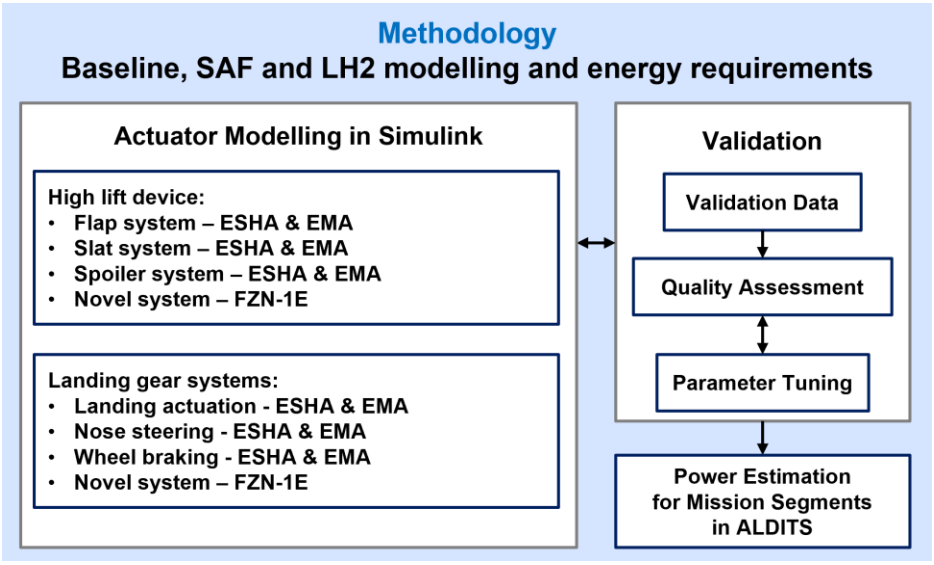


Fig. 5. Methodology for ESHA and EMA modelling.

A. High Lift Devices

The high-lift system is designed to augment lift during low-speed flight regimes such as take-off, initial climb, approach and landing. This augmentation is achieved through the deployment of leading-edge slats and trailing-edge flaps, which respectively delay flow separation and increase the effective camber and area of the wing. In addition to these devices, spoilers are multifunctional devices used for roll control and descent rate modulation during flight. During landing, they disrupt airflow over the wing to reduce residual lift, ensure firm ground contact, and support aerodynamic braking.

1. Flap and Slat

The A320 aircraft's high-lift system incorporates two trailing edge flaps and five leading edge slats on each wing. The configuration of these aerodynamic surfaces is governed by a control lever, which transmits discrete position demands to the Slat Flap Control Computers (SFCCs) via an integrated Command Sensor Unit. Each Power Control Unit (PCU) comprises two independent hydraulic motors, each powered by a separate hydraulic circuit and equipped with an individual valve block and pressure-off brake. These motors transmit rotational energy through a differential gearbox, after which torque shafts and associated gearboxes convey the mechanical power to the actuators, enabling precise positioning of the high-lift surfaces. The high-lift actuation architecture of the A-23 Theseus adopts a fully electric approach in line with More-Electric Aircraft (MEA) design philosophy. In this architecture, planetary roller screw mechanism and brushless DC permanent magnet motors are implemented for both flap and slat, reducing system mass and removing hydraulic routing. Each actuator is individually powered, offering modularity and simplified maintenance compared to centralised hydraulic systems. The flap and slat configurations typically mirror the baseline design in panel count and kinematics to facilitate direct comparison, but the actuation and power electronics represent a shift towards MEA-compliant architecture. Conversely, hydrogen-powered aircraft, particularly those developed under the FlyZero programme (e.g., FZN), require a fundamentally different approach to high-lift system integration. Due to the repositioning of fuel tanks to the fuselage and the elimination of wing-mounted kerosene tanks, the wings are 'dry', enabling internal installation of high-lift actuation components. This design allows for cleaner aerodynamic surfaces by removing external fairings and linkages, thereby reducing parasitic drag. In order to retain the capability for inboard hybrid laminar flow control suction systems during cruise, the configuration requires a morphing leading edge or slats combined with blown morphing flaps, actuated by EMAs.

In the baseline configuration, the relationship between actuator stroke and surface travel was determined by analysing the geometric layout of the flap and slat deflection mechanisms. This analysis established the linkage dynamics between the actuator and control surface, accounting for mechanical gearing and transmission ratios. Figure 6 presents the outcome of this investigation. Approximately 5% of the fairing components are located beneath the flap surface, prompting a detailed evaluation of the flap actuation system and its mechanical integration. In contrast, the slat mechanism operates via a rack-and-pinion system, exhibiting a linear displacement profile with respect to actuator stroke.

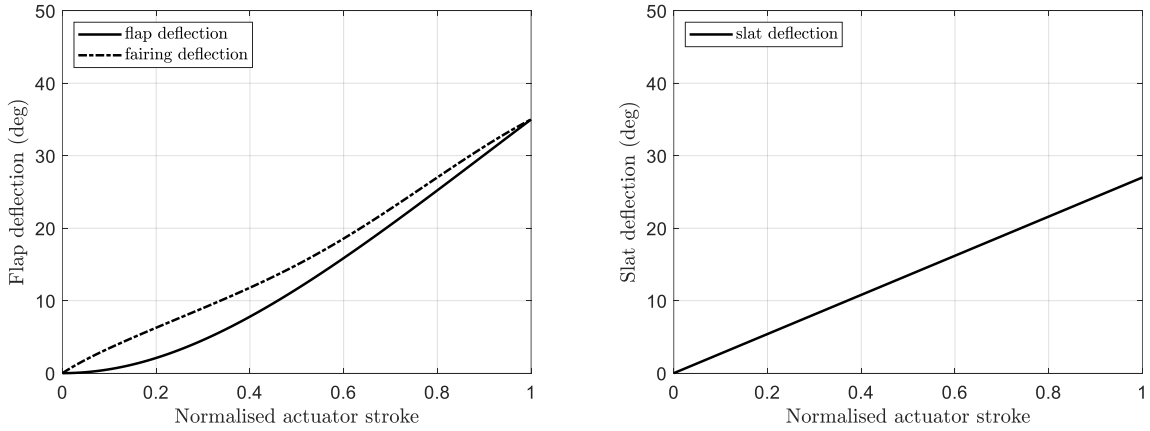


Fig. 6. Flap and slat linkage dynamics between actuator stroke and surface deflection

For modelling purposes, the differential gearbox was represented using a constant efficiency value, and a dedicated load model was formulated. This model incorporates variations in lift and drag coefficients resulting from surface extension and retraction, with coefficient estimations derived from empirical data [12]. The resulting aerodynamic load is expressed as a function of deflection angle, airspeed, and angle of attack. The ESHA and EMA characteristics for both slats and flaps were calibrated against representative typical load, actuation rate, and power requirements. Figures 7 and 8 illustrate the corresponding load, power, and energy responses for slats and flaps in response to commanded deflection angles under varying load conditions between FLAP 1+F and 2. The A320-like baseline configuration shows the highest actuation power and energy consumption, while the LH_2 configuration consistently exhibits the lowest. However, the mass penalty associated with integrating morphing actuators is non-trivial, and its aircraft-level impact must be carefully evaluated to balance energy efficiency with system weight and integration complexity.

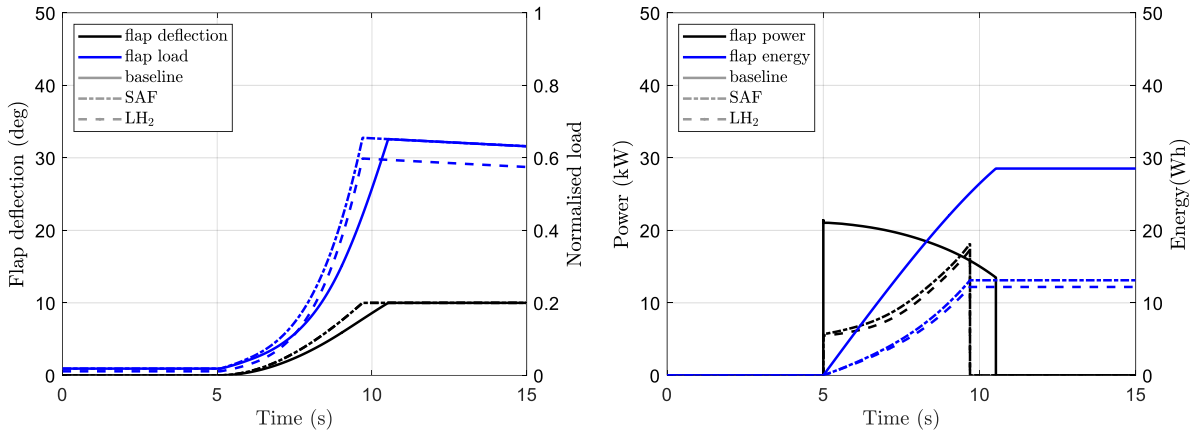


Fig. 7 Load, power and energy responses of flaps to a step input

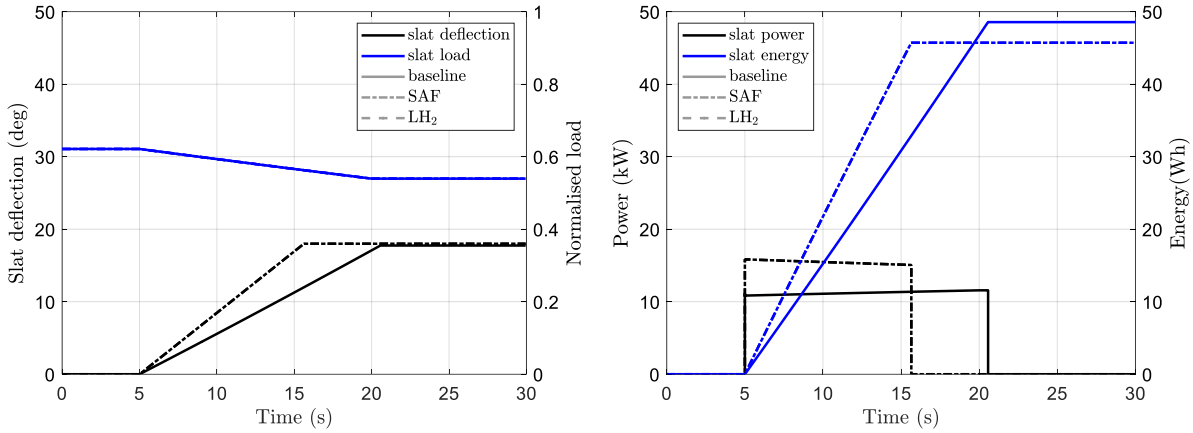


Fig. 8. Load, power and energy responses of slats to a step input

2. Spoiler actuator

Spoilers serve dual functions: acting as speed brakes during flight and as lift dumpers on the ground. In A320, these functions are managed by the Spoiler Elevator Computer (SEC), which controls spoiler deployment. Once specific logical conditions are satisfied—such as weight-on-wheels or throttle idle signals—the SEC issues deflection commands to spoilers 1 through 5. The commanded deflection angle depends on the extension status of the main landing gear struts, resulting in either a partial extension to 10° or full deployment to 50° for maximum lift dumping. For the future aircraft configurations, this critical function is achieved through the deployment of all spoiler surfaces, with each surface independently driven by an individual EMA. An analysis of the spoiler deflection mechanism reveals the relationship between surface travel and actuator stroke, governed by the underlying linkage dynamics and gearing ratios. This relationship was established to characterise the mechanical response of the system during deployment. The results are illustrated in Figure 9, which highlights the synchronised motion between the spoiler surfaces and their respective actuators.

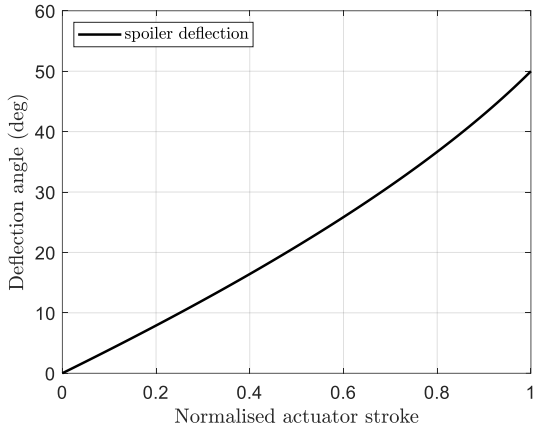


Fig. 9. Spoiler linkage dynamics between actuator stroke and surface deflection

The spoiler load model was developed by deriving lift and drag coefficients from empirical data [13-14]. Incorporating the linkage dynamics, the actuator characteristics were calibrated to reflect representative values of load, actuation rate, and power. Figures 10 and 11 and present the resulting power and energy response profiles, corresponding to surface deflection commands during a deceleration from 350 to 330 knots at a constant angle of attack. As spoilers deploy, the actuator load decreases due to the misalignment between the load axis and the airflow, which reduces the force opposing the actuator motion. Spoilers 4–5 require higher power input, as they also support roll control. Among the configurations, the baseline system shows the highest energy consumption, while the LH_2 configuration consistently demonstrates lower energy demand, attributed to its EMA implementation.

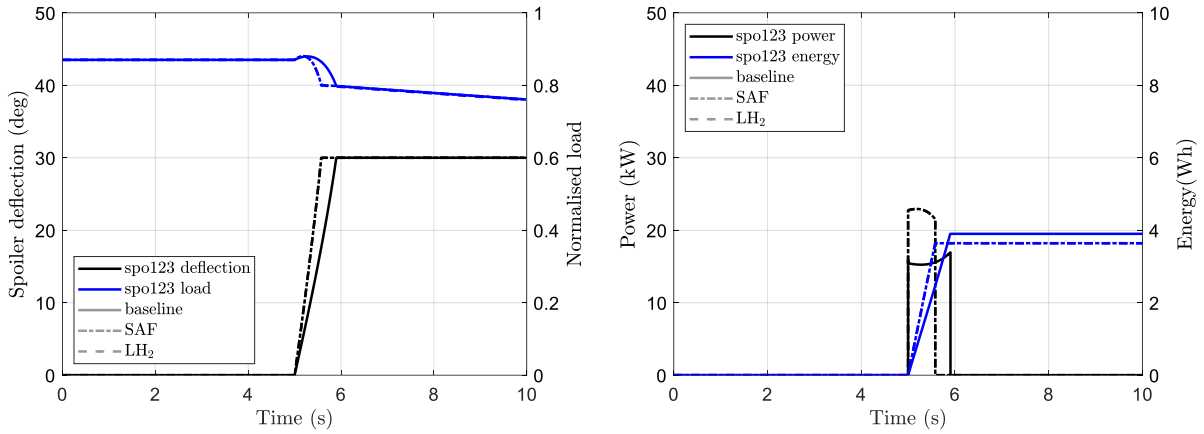


Fig. 10. Spoiler 1-3 load, power and energy responses to a step input

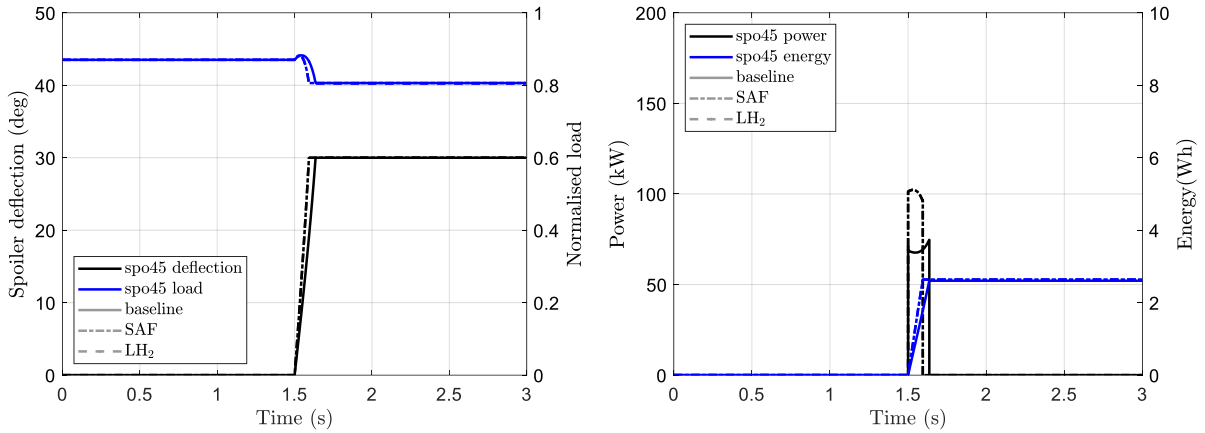


Fig. 11. Spoiler 4-5 load, power and energy responses to a step input

B. Landing Gear System

1. Landing Gear Actuator

The landing gear system of the A320 consists of a forward-retracting nose landing gear (NLG) and inboard-retracting main landing gear (MLG). Although the current study does not include the door actuators, empirical engineering references highlight their importance, and their inclusion is planned for a future study. Both the nose and main gear utilise double-acting actuators for extension and retraction. To model the linkage dynamics between the actuator and landing gear strut, geometric data were extracted from schematics. By solving the kinematic equations governing the linkage mechanism, the relationship between actuator stroke and strut extension angle was determined. As shown in Figure 12, this relationship is approximately linear for both the MLG and NLG, indicating that the effective gearing ratio induced by linkage dynamics remains nearly constant throughout the motion. Based on this observation, mean gearing ratio values of 0.1333 for the main gear and 0.1206 for the nose gear were selected for subsequent load analysis during gear extension and retraction phases. Given that the A-23 Theseus and FZN-1E aircraft have not yet reached the detailed design stage for their landing gear systems, the same actuator characteristics and modelling assumptions are applied to both configurations.

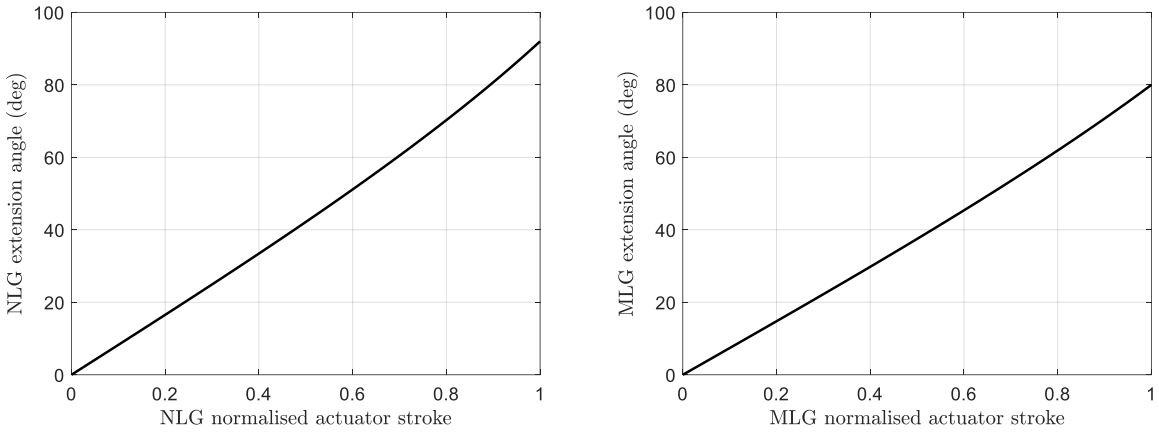


Fig. 12. MLG and NLG linkage dynamics between actuator stroke and surface deflection

For a more detailed assessment of power variation during landing gear actuation, the study examined the primary contributors to actuator loading: the weight of the landing gear and aerodynamic drag. According to the reference [15], gear weight was estimated empirically using Equations 1 and 2, while aerodynamic drag was derived following the methodology outlined in reference [15]. Since the MLG retracts laterally, crosswind components of a few degrees may influence the drag-induced load. The resulting estimations, summarised in Table 2, are consistent with empirical data indicating that landing gear weight ranges from 3.8% to 4.5% of the aircraft gross mass [15], and a drag coefficient of 0.0183. To examine maximum actuator loading, an airspeed of 230 knots was selected, representing the FLAP 1 flight condition during a landing scenario. The resulting actuator loads, plotted as functions of strut extension angle for both the NLG and MLG, are presented in Figure 13. The analysis indicates that the NLG actuator experiences a peak load of approximately 50 kN, while the combined load on the two MLG actuators reaches approximately 225 kN.

$$m_{NLG} = 20 + 0.10 m_{MTOW}^{3/4} + 2 \times 10^{-6} m_{MTOW}^{3/2} \tag{1}$$

$$m_{MLG} = 40 + 0.16 m_{MTOW}^{3/4} + 0.019 m_{MTOW} + 1.5 \times 10^{-5} m_{MTOW}^{3/2} \tag{2}$$

Table 2 Estimation and validation of both landing gear weight and drag coefficient

Parameters	Nose landing gear	Main landing gear	Total
Weight estimation	506 kg	1225 kg	2956 kg
Weight validation	N/A	N/A	2793 to 3308 kg
Drag coefficient estimation	0.0028	0.008	0.0188
Drag coefficient validation	N/A	N/A	0.0183

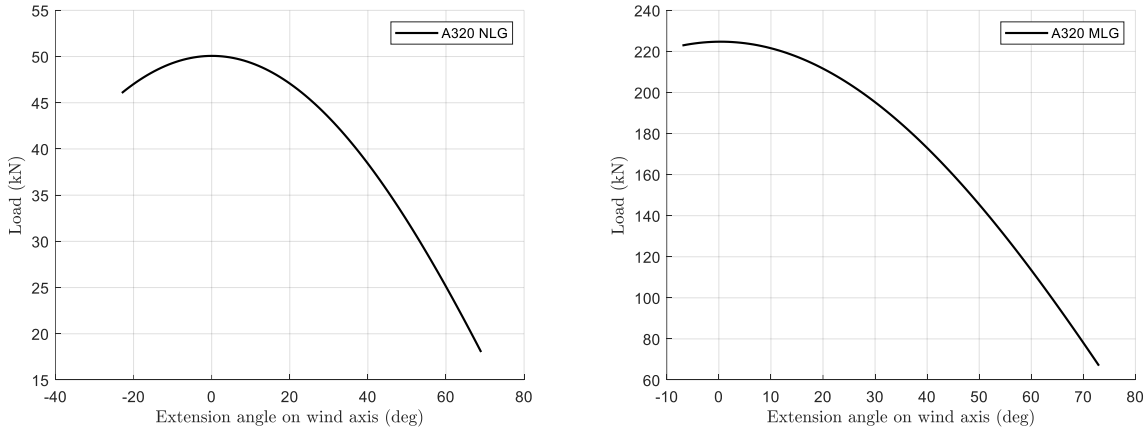


Fig. 13. NLG and MLG actuator load versus strut deflection angle

To determine the necessary power for landing gear extension and retraction, typical actuator loads and rates were analysed. The typical load was estimated under the FLAP 2 flight condition, as landing gear deployment primarily occurs during this configuration [23]. Based on these load values, actuator characteristics were tuned to achieve typical actuation speeds of 7.1°/s for NLG and 6.0°/s for the MLG. These speeds correspond to extension and retraction times of approximately 13 seconds, consistent with the study in [23], considering rotation ranges of 92° for the NLG and

80° for the MLG. The nominal landing gear retraction time is approximately 7 seconds; however, this duration may increase under elevated load factor (G-level) conditions. The resulting typical power requirements were calculated as 6.2 kW for the NLG and 18.3 kW for the MLG.

To validate these estimates, a hydraulic fluid kinematic approach was employed by extracting the actuator displacement and piston area from landing gear schematics. The method was corroborated by estimating the actuation power for the A380 landing gear system, for which published data report a value of 175 kW [16]. Using the same technique, the estimated value was 167 kW, corresponding to a deviation within 5%. For the A320-like narrow-body aircraft, the computed average power was 43 kW, comprising 7 kW for the NLG and 36 kW for the MLG, which deviates by approximately 9% from the initial estimates. Based on these validated results, actuator power characteristics were adjusted to match the required power under typical load conditions.

Given that landing gear extension is typically executed at FLAP 2 configuration, the corresponding power and energy characteristics in response to a gear extension step input are shown in Figures 14 and 15. The NLG load profile varies dynamically, peaking near mid-extension due to combined aerodynamic and gravitational effects. In contrast, the MLG load decreases progressively, reaching up to 20% reduction from its maximum value as weight-induced loading is alleviated through the retraction arc. Among the three configurations, the A320-like baseline requires the highest actuation energy, while the LH_2 configuration consistently demonstrates the lowest power and energy demands, attributable to its reduced mass and lighter landing gear structure.

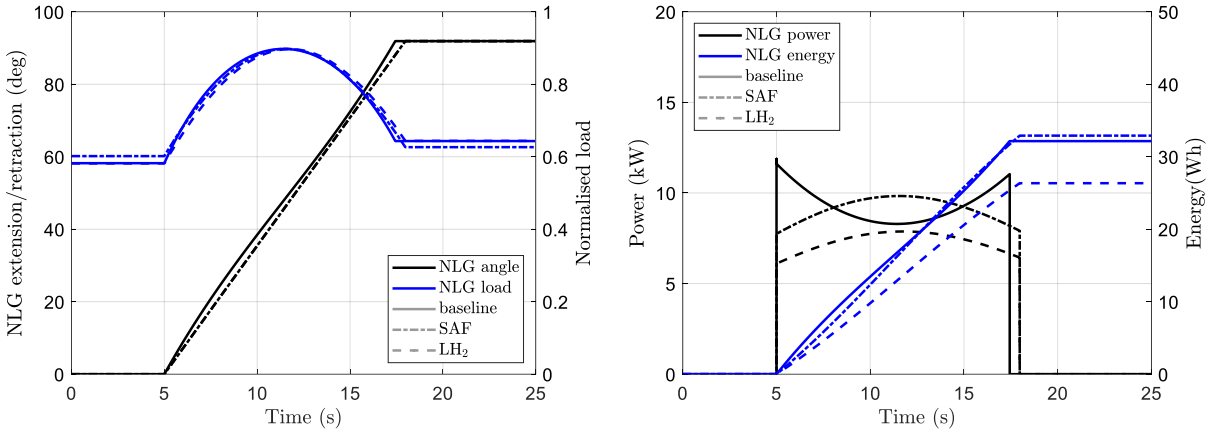


Fig. 14. NLG load, power and energy responses to an extension step input

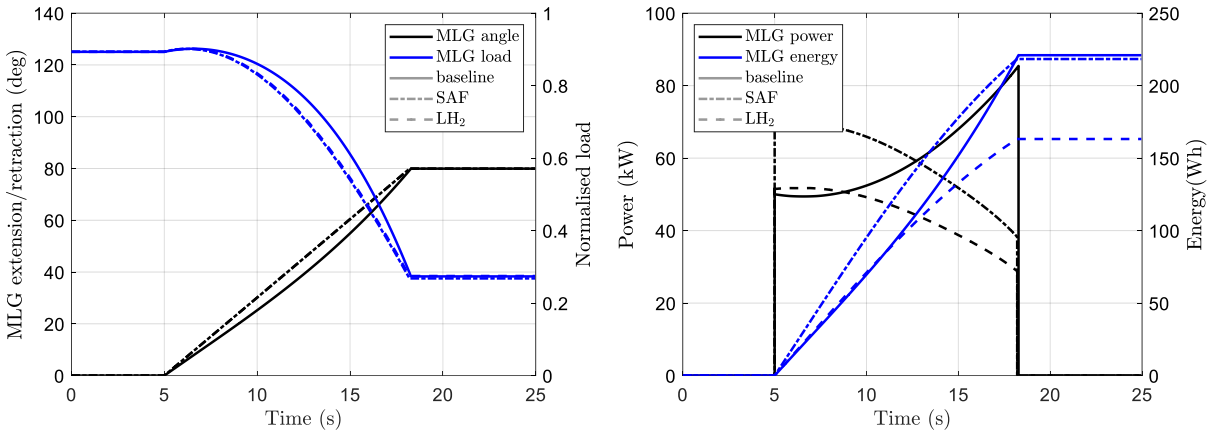


Fig. 15. MLG load, power and energy responses to an extension step input

2. Nose Steering Actuator

The nose wheel steering system is electrically actuated and controlled via the Braking and Steering Control Unit (BSCU), receiving input from the cockpit through a combination of rudder pedals and handwheels. Input authority is velocity-dependent, with rudder pedals typically dominating at higher speeds. The two-wheel nose gear includes a steering actuator that drives a rotating tube—a structural element of the nose landing gear—via a rack-and-pinion mechanism. While a rigorous evaluation of rack-and-pinion performance would ideally require force and linear velocity profiles, the current power estimation is based on torque and angular velocity, as the linkage between actuator output and steering angle is approximately linear. Additionally, the efficiency difference between rotational and translational modelling approaches is estimated to be less than 7% [17]. Therefore, the steering actuator load and power demands are reasonably approximated using a torque-based formulation. As the A-23 Theseus and FZN-1E aircraft have not progressed to the detailed design phase for their nose wheel steering systems, the A320 steering actuator specifications [16], incorporating EMA characteristics, are adopted as the basis for modelling and comparative analysis. Table 3 presents the performance characteristics of the nose landing gear steering actuator. In modelling the steering actuator, the approach adjusts an ESHA and EMA characteristics diagram that satisfies the requirement of a 20 deg/s steering rate and a steering actuator power of 1.4 kW at 4000 Nm, while also ensuring a zero rate at the maximum load.

Table 3 Nose steering actuator characteristics

Actuation function	Nose landing gear steering
Steering angle	$\pm 75°$
Speed at load of 4000 Nm	$20°/\mathrm{sec}$
Maximum load	7000 Nm

It is important to recognise that both the steering load and actuation rate vary as functions of steering angle and taxiing velocity. To account for these dependencies, a detailed load modelling exercise was conducted following the methodology outlined by D.W. Young [18]. The steering torque is primarily influenced by four contributing moments, expressed in Equation 3: the flat spot effect, rolling resistance on a curved path, rolling drag due to scrubbing, and the resisting torque from the main landing gear. Assuming a representative taxi speed of 30 knots, the resulting steering torque profile as a function of steering angle is shown in Figure 16.

With the load model augmented, power and energy responses to the steering angle step input were evaluated for the three aircraft configurations, as shown in Figure 17. The simulation accounted for varying load conditions due to a decrease in airspeed from 30 to 20 knots, during which the imposed steering torque changes accordingly. As a result, steering power demand ranged between approximately 2 and 3 kW. Minor differences were observed between the SAF and LH_2 configurations, primarily attributed to variations in aircraft mass and wing area. The LH_2-based system exhibited approximately 3% lower power consumption compared to the SAF counterpart, owing to slightly reduced steering loads.

$$M_{\text{steering}} = M_{\text{rolling}} + M_{\text{tyre}} + M_{\text{drag}} + M_{\text{sideload}}$$

where

$$\begin{aligned} M_{\text{rolling}} &= \mu \cdot F_z \cdot D_{\text{LG}} \\ M_{\text{tyre}} &= 0.24 F_z \cdot B^2 / D_{\text{LG}} \\ M_{\text{drag}} &= (\mu \cdot F_z - T_{\text{idle}}) \cdot D_{\text{LG}} \cdot \sin\theta_{\text{steering}} \\ M_{\text{sideload}} &= S \cdot D_{\text{LG}} \cdot \cos\theta_{\text{steering}} \end{aligned} \tag{3}$$

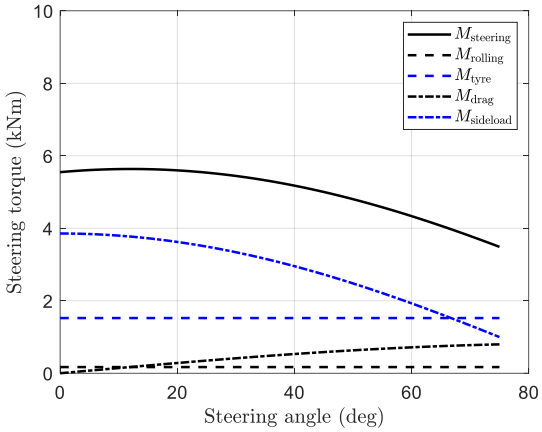


Fig. 16. Steering torque load with varying steering angle

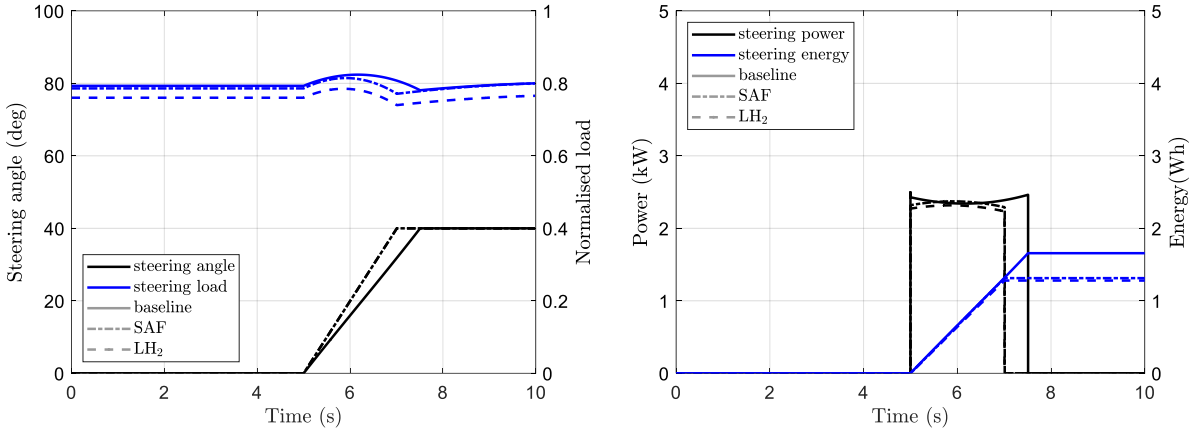


Fig. 17. Steering load, power and energy responses to a step input

3. Wheel Brake

The A320 is equipped with carbon multidisc brakes on each of the two wheels of the main landing gear. Brake commands are initiated electrically via pedal input and processed by the Braking and Steering Control Unit (BSCU). The BSCU activates a selector valve, enabling hydraulic pressure to be routed to the brakes through the automatic selector and standard servo valves. Each main wheel is also fitted with anti-skid functionality to enhance braking effectiveness. Braking torque is controlled through brake pressure with system pressures ranging from 0 to 3000 psi. Table 4 presents the applied brake pressures alongside their associated target deceleration rates. The use of the auto-brake system is recommended for consistent deceleration performance and offers three selectable modes: MAX, MED, and LO. The MAX setting is typically engaged for rejected take-off scenarios, while MED and LO are used during landing, corresponding to deceleration targets of 0.3g and 0.17g, respectively.

Referring to the study [20], Figure 18 illustrates the relationship between deceleration rate and applied brake pressure on the carbon disc. The relationship assumes closed-loop brake control following this characteristic; however, the actual response may vary depending on factors such as brake dynamics, aircraft mass, and runway conditions. The curve exhibits an initial dead zone up to approximately 1000 psi, during which pressure increases do not result in effective deceleration. This behaviour occurs because the piston is in motion but has not yet contacted the brake disc, leaving a mechanical gap. Once this gap is closed, the system enters the working zone, where further increases in pressure produce a corresponding rise in deceleration due to direct force transmission through the brake stack. Since the A-23 Theseus and FZN-1E aircraft have not yet reached the detailed design stage for their wheel brake systems,

both are assumed to adopt the A320 brake system philosophy, implemented through EMA characteristics, for the purposes of modelling and comparative analysis.

Table 4. A320 autobrake modes and deceleration rate

Autobrake selector	Applied brake pressure	Deceleration rate	Note
LO	1250 psi	$1.7\ \mathrm{m/s^2}$	-
MED	2500 psi	$3.0\ \mathrm{m/s^2}$	-
MAX	3000 psi	$3.5\ \mathrm{m/s^2}$	RTO

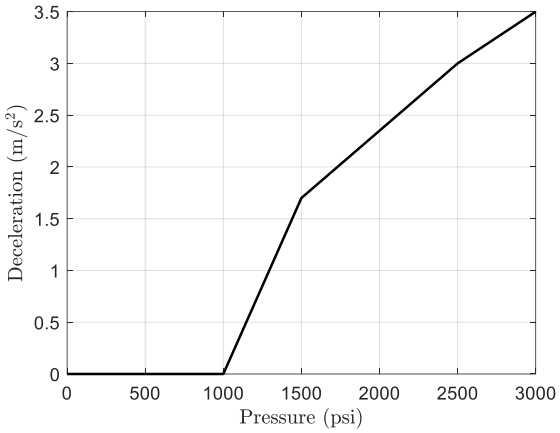


Fig. 18. Brake pressure–deceleration relationship for A320-like main landing gear system

Even though a dead zone is present, the system typically reaches full brake pressure within approximately 0.3 seconds, based on typical hydraulic flow rates and brake line volumes. As a result, the detailed dynamics associated with piston displacement are considered negligible in the actuator modelling. When anti-skid is active, aircraft-level brake power can reach up to 10 kW. Accordingly, a peak power value of 10 kW at 3000 psi was used to calibrate the ESHA and EMA power trend curve. The actuator stroke rate was also tuned to achieve full pressure within the 0.3 second interval. It is important to note that the assumption of no anti-skid activation is generally valid for most landing scenarios; however, in conditions involving wet runways or heavy braking with a lightly loaded aircraft, anti-skid operation would increase the overall brake power demand.

Figure 19 shows power response of the wheel brake system to a step deceleration input for three aircraft configurations. Following the step command at 0.5 seconds, the pressure builds up with a short lag, reaching its target value just after 0.6 seconds. When it comes to brake power and cumulative energy consumption, the baseline configuration exhibits the highest initial brake power demand due to efficiency losses inherent in the hydraulic system, followed by SAF and LH_2. This variation reflects differences in each actuator characteristics.

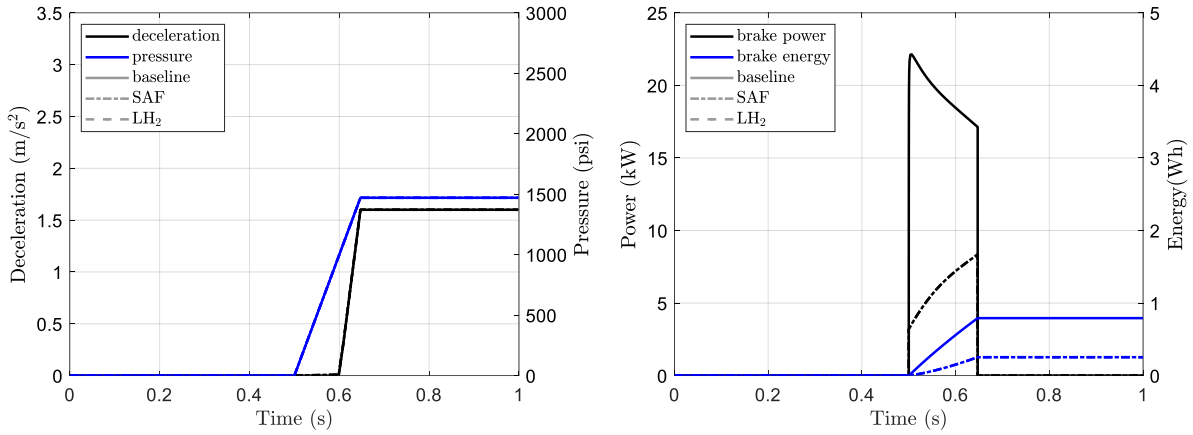


Fig. 19. Wheel brake power and energy responses to a deceleration step input

V. Terminal Phase Simulation

This section covers the estimation of power and energy requirements for the terminal phase flight, with particular focus on control surfaces and landing gear systems. All pertinent models have been assimilated within modified ALDITS.

A. Actuator Command Profile

1. Flap and Slat

Table 5 presents the slat and flap deployment schedule during terminal mission segments, correlating secondary control surface deflections with their limiting speeds, defined as Velocity Flap Extended (VFE), and associated flight phases. During cruise, both slats and flaps remain fully retracted at Position 0. At Position 1, the slats are deflected to 18°, while flaps remain at 0°, with a maximum permissible speed of 230 kts, typically used during early descent. Position 1+F retains the slat deflection at 18° and introduces a 10° flap extension, suitable for take-off or operation below 215 kts to enhance lift. As the aircraft transitions to final approach and landing, the high-lift surfaces are progressively extended, reaching 27° for slats and 35° for flaps at the Full position, with a reduced VFE of 177 kts.

Table 5. Position of slats and flaps in the terminal mission segments

Position	Slats	Flaps	VFE	Flight phases
0	0°	0°	VMO/MMO	Cruise
1	18°	0°	230 kts	
1+F	18°	10°	215 kts	Take off
2	22°	15°	200 kts	Approach
3	22°	20°	185 kts	Landing
Full	27°	35°	177 kts	

2. Spoiler Actuator

Spoiler actuators remain active during flight to support both load control and lift damping, particularly during approach. For load control purposes, all spoilers are deflected to 50 degrees on eight separate occasions, while spoilers 4 and 5 are deflected to 10 degrees four times. During landing, lift dumpers become aerodynamically effective approximately 1.5 seconds after touchdown, after which full spoiler deflection is achieved.

3. Landing Gear Actuator

Landing gear is retracted within 3–5 seconds after takeoff to reduce drag and improve climb performance. This action is initiated once a positive rate of climb is established, generally around 200 feet above ground level (AGL). Retraction occurs while the aircraft is in the FLAP 2 configuration.

4. Steering

A recent study based on Euro Control's extranet has unveiled that the typical taxi-out and taxi-in durations for the A320-200 on terrestrial grounds amount to approximately 15 minutes and 6 minutes, respectively [19]. For the purposes of ground terminal phase simulation, two pieces of flight radar data approximating these average durations were chosen. The resulting terminal phase profiles, which capture variations in ground speed and heading, are illustrated in Figures 20 and 21. Equation 4 was employed to determine the required steering angle to achieve the desired heading change.

$$\delta_{\text{steering}} = \text{atan}\left(\Delta\theta_{\text{heading}} L_{\text{wheelbase}} / d_{\text{travel}}\right) \tag{4}$$

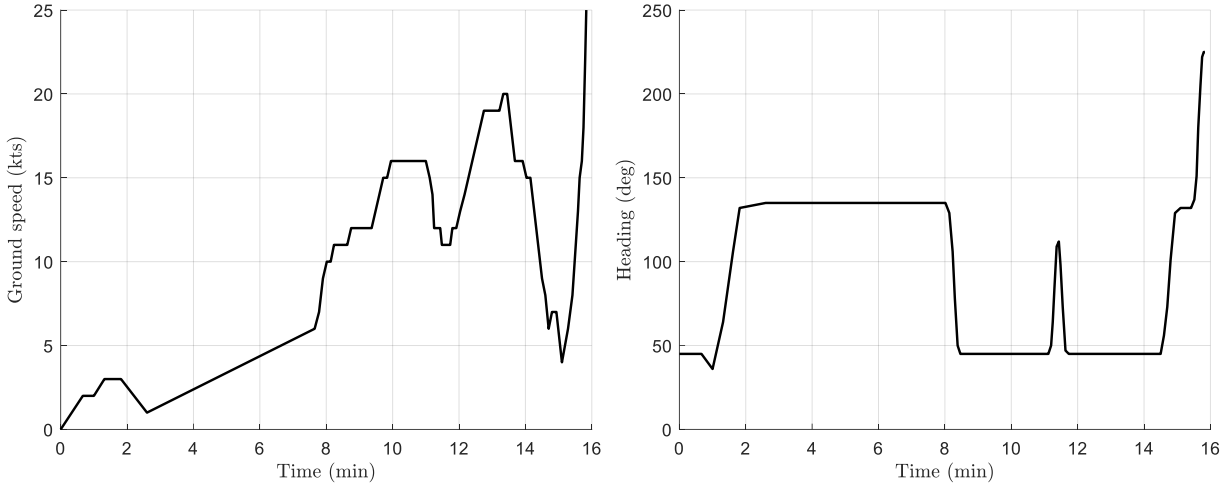


Fig. 20. Taxi-out ground mission profile

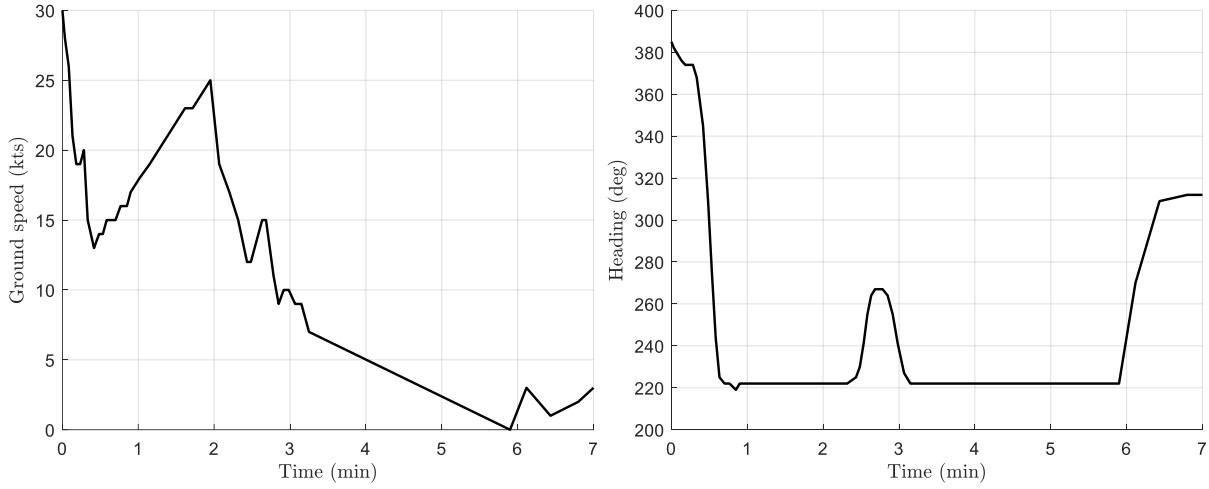


Fig. 21. Taxi-in ground mission profile

5. Brake Actuator

Apart from brake use during taxi operations, landing-phase deceleration relies primarily on the wheel brake system. The aircraft deceleration is governed by four dominant forces: aerodynamic drag, thrust reverser, rolling friction, and wheel brake force. To determine the brake command required, it is necessary to compute the wheel brake force as the

residual after accounting for all other deceleration contributions. Assuming LO autobrake mode, the total deceleration force can be expressed as shown in Equation 4, with individual components modelled separately. The aerodynamic and weight-dependent terms vary by aircraft configuration, while reverse thrust force and its time profile were estimated based on the study [22]. Rolling resistance was calculated using the effective normal force and a rolling friction coefficient of 0.015 as referenced in [21]. Regarding weight distribution for rolling friction force estimation, the main landing gear supports approximately 85–92% of the total weight during landing, depending on the aircraft's centre of gravity position [15]. For this analysis, a representative mean value was adopted as a simplification.

$$F_{brake} = 0.17m - D - \mu\eta_{MLG}(mg - L) - T_R \tag{4}$$

Under the assumption that the aircraft decelerates from 130 to 30 knots, Figure 22 presents an example of the baseline configuration deceleration breakdown. The net deceleration force required remains nearly constant, corresponding to the target deceleration rate. The other curves represent aerodynamic drag (black solid), thrust reverser over 10 seconds, and rolling resistance. The required wheel brake force is obtained by subtracting the sum of these passive contributions from the total required force. The observed discrepancies between configurations are primarily attributed to differences in airframe geometry and aircraft mass, which affect aerodynamic drag, rolling resistance, and inertia during deceleration.

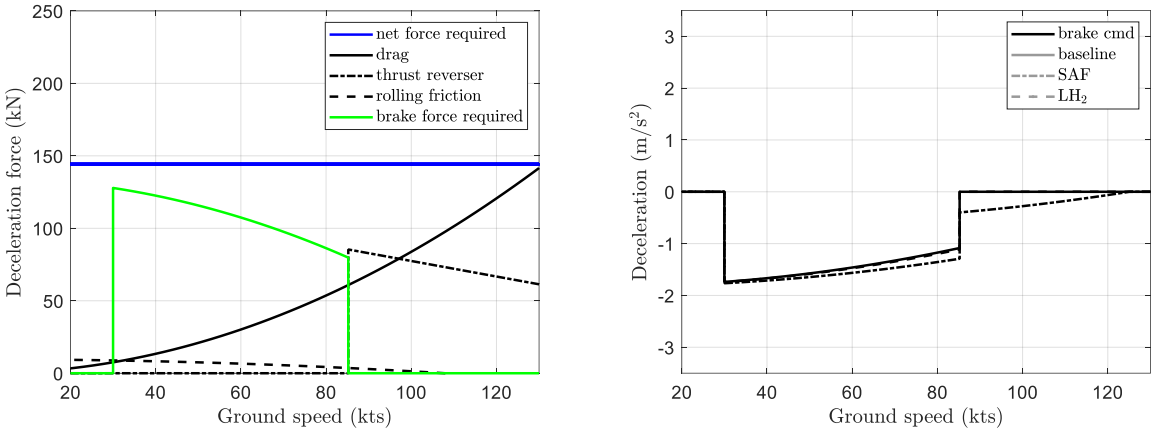


Fig. 22. Deceleration force breakdown and command profile for wheel brake assembly

B. Terminal Phase Simulation

Figure 23 presents the total actuator power and energy consumption over a simplified whole mission profile for the A320-like baseline, SAF, and LH_2 aircraft configurations. The black lines represent instantaneous power, while the blue lines indicate cumulative energy. Overall, it was found that the landing phase demands more energy than the take-off phase, with the energy consumption during take-off amounting to approximately 20% of that required for landing. Two distinct power spikes are observed—one shortly after take-off and another just before landing—corresponding to landing gear retraction and extension, as well as deployment of secondary control surfaces, followed by the remaining actuators. The energy curves plateau during cruise since the analysis is focused on terminal flight phases, where actuator activity is concentrated. Among the three configurations, the baseline exhibits the highest cumulative energy usage at approximately 3,118 Wh, followed by the SAF configuration at around 911 Wh, while the LH_2 configuration shows the lowest consumption at approximately 737 Wh, emphasising the energy-saving advantages of more-electric system architectures.

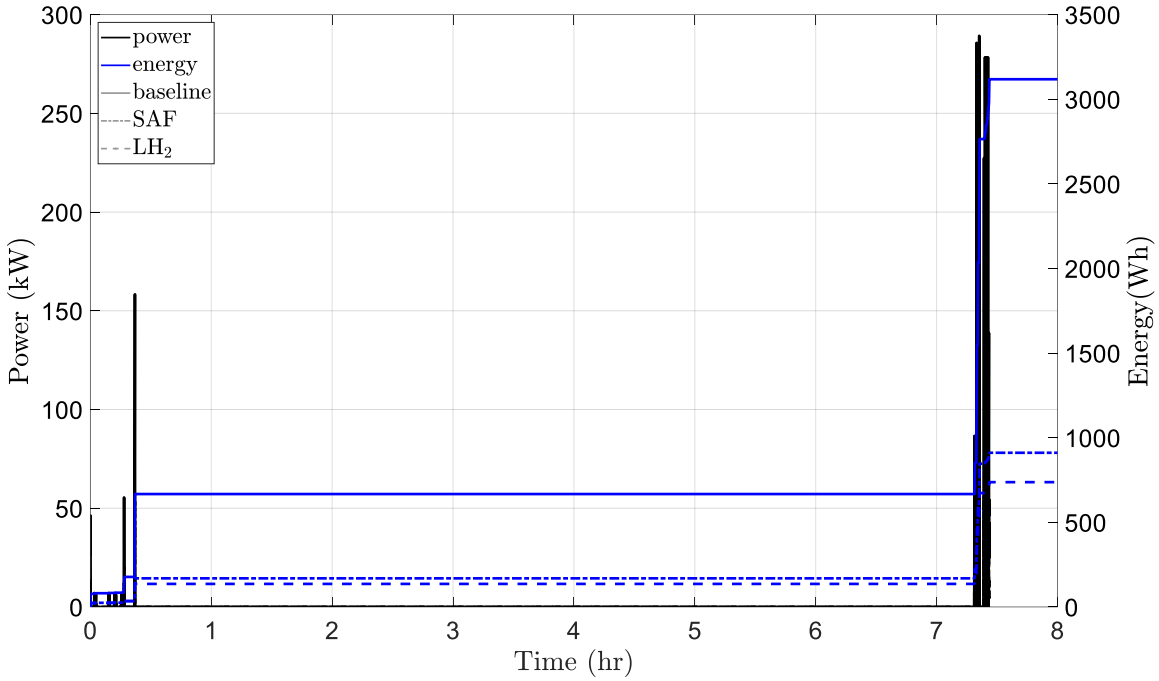


Fig. 23. Total actuator power and energy consumption over a complete mission profile

VI. Conclusions

This study presented a comparative assessment of actuator energy requirements during terminal operations for three single-aisle aircraft configurations: a conventional hydraulic A320-like baseline, a SAF-powered more-electric aircraft, and an LH_2-powered zero-emission concept. By developing detailed load and actuation models across secondary flight control systems, landing gear, and braking assemblies, the analysis captured power and energy profiles under representative mission conditions. Results reveal that the baseline aircraft consistently demands the highest cumulative actuator energy—approximately 3,118 Wh—primarily due to hydraulic inefficiencies. The SAF configuration reduces this demand by 70%, while the LH_2 platform further lowers it to around 737 Wh, benefiting from lighter structures and fully electric actuation. However, while the LH_2 system shows clear energy efficiency advantages, the non-negligible mass and integration complexity associated with novel actuators like morphing surfaces must be addressed at the aircraft level. Future work will extend the analysis to system-level trade-offs, incorporating more detailed actuator architectures for future aircraft concepts and fuel consumption across complete mission segments.

Acknowledgments

This research was funded by Innovate UK grant number 10002411, under the ATI/IUK Project: LANDOne, with Airbus UK as Industrial Lead.

References

1. Jensen, L.L., Bonnefoy, P.A., Hileman, J.I. and Fitzgerald, J.T., “The Carbon Dioxide Challenge Facing US Aviation and Paths to Achieve Bet Zero Emissions by 2050,” *Progress in Aerospace Sciences*, Vol. 141, 2023, p.100921.
2. Tom, L., Khowja, M., Vakil, G. and Gerada, C., “Commercial Aircraft Electrification—Current State and Future Scope,” *Energies*, Vol. 14, No. 24, 2021, pp.8381. doi: 10.3390/en14248381

3. Mazzoleni, M., Di Rito, G., and Previdi, F., "Electro-Mechanical Actuators for the More Electric Aircraft," Cham, Switzerland, Springer, 2021
4. Reeder, J. P., Taylor, R. T., and Walsh, T. M., "New Design and Operating Techniques and Requirements for Improved Aircraft Terminal Area Operations," Tech. Rep. NASA-TM-X-72006, 1974.
5. Senzig, D. A., Fleming, G. G., & Iovinelli, R. J., "Modeling of Terminal-Area Airplane Fuel Consumption," Journal of Aircraft", Vol. 46, No.4, 2009, pp.1089-1093. https://doi.org/10.2514/1.42025
6. Cooper, M. A., "Simulating Actuator Energy Demands of an Aircraft in Flight," Doctoral dissertation, Cranfield University, School of Engineering, 2014.
7. Chakraborty, I., Mavris, D. N., Schneegans, A., and Emeneth, M, "An Integrated Approach to Vehicle Propulsion System, and Subsystem Sizing-Application to the All-Electric Aircraft," *Proceedings of the Institution of Mechanical Engineers, Part G: Journal of Aerospace Engineering*, Vol. 230, No.3, 2010, pp. 496-514. https://doi.org/10.1177/0954410015594399
8. Fu, J., van Heerden, A. S., Judt, D., and Lawson, C., "A Generic Mission-Level Flight Control Surface EMA Power Consumption Simulation Tool," *Aerospace*, Vol.9, (6), 2022, pp.290.
9. Roskam, J., "Airplane Design," Roskam Aviation and Engineering Corp., Ottawa, KS, 1985.
10. Raymer, D. P., *Aircraft design: A Conceptual Approach*, American Institute of Aeronautics and Astronautics , Reston, VA, 2018, Chapter 16.
11. van Heerden, A. S., Judt, D. M., Lawson, C. P., Jafari, S., Nikolaidis, T., and Bosak, D., "Framework for Integrated Dynamic Thermal Simulation of Future Civil Transport Aircraft," AIAA SciTech 2020 Forum, 2020
12. ESDU, "Normal Force on Flaps and Controls," Tech. Rep. Flaps 05.01.01, Dec 1973
13. ESDU, "Lift and Drag due to Spoiler Operation in the Ground Run," Tech. Rep. 76026, 1977
14. ESDU, "Drag and Yawing Moment due to Spoilers," Tech. Rep. 96026, 2014
15. Currey, Norman S., *Aircraft Landing Gear Design: Principles and Practices*, American Institute of Aeronautics and Astronautics, 1988.
16. Maré, J. C., *Aerospace Actuators 3: European Commercial Aircraft and Tiltrotor Aircraft*, John Wiley & Sons; 2018.
17. Heinrich, M. T., Kelch, F., Magne, P., and Emadi, A., "Regenerative Braking Capability Analysis of an Electric Taxiing System for a Single Aisle Midsize Aircraft," *IEEE Transactions on Transportation Electrification*, Vol.1, (3), 2015, pp.298-307.
18. Young D.W., "Landing Gear Design," Cranfield University, 2004.
19. Pang CH., "Electrically Powered On-Board Aircraft Taxi System for Flag Carrier," Master dissertation, Cranfield University, Aug 2023
20. Long, M., and Jing, H., "Active Deceleration Control of Brake-by-Wire System," *39th Chinese Control Conference*, 2020, pp.5523-5527.
21. Horne, W. B., and Leland, J.W., *Influence of the Tire Tread Pattern and Runway Surface Condition on Breaking Friction and Rolling Resistance of a Modern Aircraft Tire*, National Aeronautics and Space Administration, 1962
22. Mahmood, T., Jackson, A., Rizvi, S. H., Pilidis, P., Savill, M., and Sethi, V., "Thrust Reverser for a Mixed Exhaust High Bypass Ratio Turbofan Engine and Its Effect on Aircraft and Engine Performance," *Turbo Expo: Power for Land, Sea, and Air*, Vol.44670, 2011, pp.205-215.
23. Deiler, C., and Fezans, N., "Modeling of the A320 Landing Gear Drag During Their Extension and Retraction," *AIAA SciTech 2025 Forum*, 2025, pp.1250.



https://dspace.org/

Energy comparison in terminal area for narrow body, SAF and LH2 aircraft

Kang, Namuk; Cha, Jihyoung; Judt, David M.; Lawson, Craig P.; Skote, Martin ...

2025-07-29
American Institute of Aeronautics and Astronautics (AIAA)
https://doi.org/10.2514/6.2025-3371
Kang N, Cha J, Judt D, et al., (2025) Energy comparison in terminal area for narrow body, SAF and LH2 aircraft. In: AIAA Aviation Forum and Ascend 2025, 21-25 July 2025, Las Vegas, USA, Article number 2025-3371

Downloaded from a DSpace repository. https://dspace.org/